

Direct Probing of the Electronic Structures of Single-Layer and Bilayer Graphene with a Hexagonal Boron Nitride Tunneling Barrier

Suyong Jung,^{*,†,‡} Nojoon Myoung,[‡] Jaesung Park,[†] Tae Young Jeong,^{†,||} Hakseong Kim,[†] Kenji Watanabe,[⊥] Takashi Taniguchi,[⊥] Dong Han Ha,[†] Chanyong Hwang,[†] and Hee Chul Park^{*,‡}

[†]Korea Research Institute of Standards and Science, Daejeon 34113, Korea

[‡]Center for Theoretical Physics of Complex Systems, Institute for Basic Science, Daejeon 34051, Korea

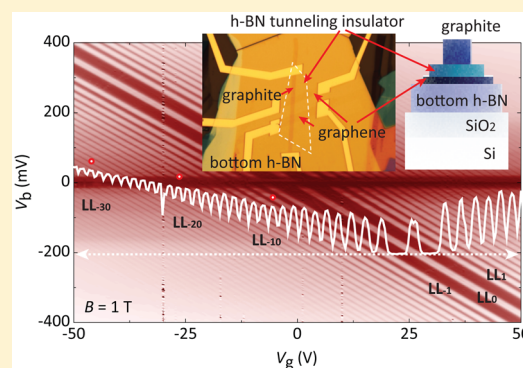
^{||}Department of Physics, Chungnam National University, Daejeon 34134 Korea

[⊥]National Institute for Materials Science, 1-1 Namiki, Tsukuba 305-0044, Japan

Supporting Information

ABSTRACT: The chemical and mechanical stability of hexagonal boron nitride (*h*-BN) thin films and their compatibility with other free-standing two-dimensional (2D) crystals to form van der Waals heterostructures make the *h*-BN-2D tunnel junction an intriguing experimental platform not only for the engineering of specific device functionalities but also for the promotion of quantum measurement capabilities. Here, we exploit the *h*-BN-graphene tunnel junction to directly probe the electronic structures of single-layer and bilayer graphene in the presence and the absence of external magnetic fields with unprecedented high signal-to-noise ratios. At a zero magnetic field, we identify the tunneling spectra related to the charge neutrality point and the opening of the electric-field-induced bilayer energy gap. In the quantum Hall regime, the quantization of 2D electron gas into Landau levels (LL) is seen as early as 0.2 T, and as many as 30 well-separated LL tunneling conductance oscillations are observed for both electron- and hole-doped regions. Our device simulations successfully reproduce the experimental observations. Additionally, we extract the relative permittivity of three-to-five layer *h*-BN and find that the screening capability of thin *h*-BN films is as much as 60% weaker than bulk *h*-BN.

KEYWORDS: Electron tunneling spectroscopy, hexagonal boron nitride, van der Waals heterostructures, Landau level tunneling spectroscopy, electric-field-induced bilayer graphene energy gap, relative permittivity of thin oxide films



Electron-tunneling spectroscopy has proven its capability in probing the novel electronic structures of solid-state systems such as the energy gap of superconducting materials^{1–3} and the Landau level (LL) formation of two-dimensional (2D) electronic systems such as InAs⁴ and graphene.^{5–7} With the advent of the scanning tunneling microscope (STM), tunneling spectroscopy measurement has expanded into the investigation of electronic structures, specifically the density of states of a specimen at atomic resolution.⁸ It is challenging, however, to employ tunneling spectroscopy measurements for nanoscale devices with limited conducting surfaces for the STM probe to navigate and extra gate electrodes with insulating layers. In addition, it is essential to have a pristine tunneling probe–insulator–specimen junction not inflicted by any electrical or chemical defects, which often alter the tunneling spectrum completely.⁹

Recently, the capability to isolate a few layers of high-quality hexagonal boron nitride (*h*-BN) and stack them in the form of 2D van der Waals heterostructures combined with other layered materials^{10,11} has made it possible to exploit electron-tunneling spectroscopy measurements for low-dimensional

nanoscale devices.^{12–15} For example, electron-tunneling devices with thin *h*-BN as a tunneling insulator demonstrate their potential for future device applications in tunneling electron transistors,¹⁴ resonant tunneling in ultrafast electronic devices,¹⁶ and light-emitting diodes.¹⁷ We have previously shown that *h*-BN–graphene tunneling devices can be implemented to probe not only the phonons of their constituents, namely *h*-BN, graphene, graphite, and the *h*-BN–graphene interface, but also other collective excitations, such as plasmons with much-improved accuracy.¹⁵ Vdovin et al. has also reported eight phonon modes from graphene–*h*-BN–graphene tunneling transistors.¹⁸ Until now, however, experimental demonstrations on probing the electronic structures of nanoscale devices with *h*-BN tunneling insulators have been sparse despite their high applicability and potential in quantum tunneling measurements.

Received: September 12, 2016

Revised: December 13, 2016

Published: December 22, 2016

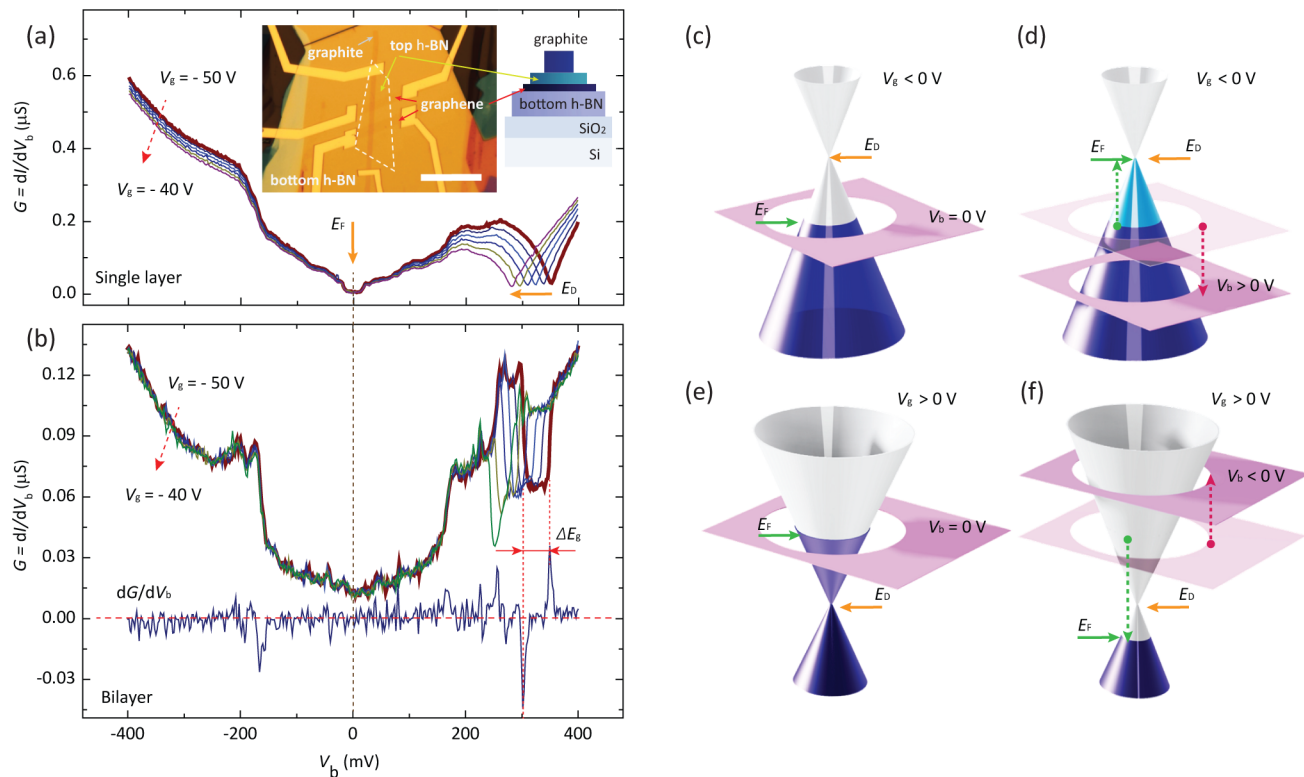


Figure 1. (a,b; inset) Optical image of one of the single-layer graphene devices with thin *h*-BN as a tunneling insulator and the schematic of a graphite-*h*-BN-graphene 2D stacks placed on the SiO₂-Si substrate (scale bar: 20 μ m). Sample bias (V_b) is applied to the top graphite probe, and tunneling current is monitored through the graphene layer. Differential conductance ($G = dI/dV_b$) versus V_b measured from $V_g = -50$ V (bold line) to $V_g = -40$ V with a spacing of $\Delta V_g = 2$ V and $T = 5.0$ K for the (a) single and (b) bilayer graphene devices. The Dirac point (E_D in (a)) and the electric field-induced bilayer energy gap (E_g in (b)) are marked for the single-layer and bilayer graphene devices, respectively. Conductance derivative (dG/dV_b) is numerically obtained from the spectrum at $V_g = -50$ V. Spectra gap boundaries are located from Lorentzian fittings of the peak and dip in the dG/dV_b plot. (c–f) Schematics of energy-band alignments of graphene and graphite probes: (c) hole-doped ($V_g < 0$ V) region at $V_b = 0$ V; (d) $V_b > 0$ V, where the Fermi level of graphene (E_F) is aligned at E_D ; (e) electron-doped ($V_g > 0$ V) region at $V_b = 0$ V; (f) $V_b < 0$ V, where E_F is positioned below E_D . Note that the position of E_F is modulated by changing V_b at the graphite probe. Purple planes indicate the Fermi level positions of the graphite probe.

In this article, we focus on probing the electronic structures of gated single- and bilayer graphene devices by electron tunneling spectroscopy with thin *h*-BN as a tunneling insulator. For single-layer devices, the charge neutrality point (Dirac point, E_D) can be identified in the tunneling spectra as a sharp dI/dV_b dip at zero magnetic field. Upon increasing the external magnetic field, the development of LLs is seen as early as 0.2 T, with as many as $LL_N = \pm 30$ as a Landau level index (LL_N) observed for both electron- and hole-doped regions. We attribute this excellent signal-to-noise ratio to much-improved *h*-BN-graphene tunneling junctions, compared with previous tunneling studies on graphene devices.^{9,19–21} For bilayer devices, we are able to detect the development of the bilayer energy gap as a function of back-gate (V_g) and sample-bias (V_b) voltages for the first time with quantum tunneling measurements. The electric-field-induced bilayer energy gap (E_g) formed at the charge neutrality point increases in size as the electric field between the top and bottom layers increases. Our device simulations successfully reproduce the experimental observations with a direct approach of electrostatic interactions between the graphite probe and graphene through the *h*-BN tunneling insulator. Finally, we extract the relative permittivity (DC permittivity) of multiple thin *h*-BN films (three to five layers), where it is seen that the screening capability of thin *h*-BN films is as much as 60% weaker than the value of bulk *h*-BN.

As displayed in the inset of Figure 1a, our single and bilayer graphene is sandwiched by both a thick back-gate (>20 nm) and thin tunneling insulator (1.0–1.8 nm) *h*-BN flakes. V_b is applied to the graphite probe (thickness >10 nm) placed on top of the thin *h*-BN, and both tunneling current and differential conductance ($G = dI/dV_b$) are measured through the graphene layer. It is demonstrated that the tunneling spectra, especially $G = dI/dV_b$, represent the electronic structures of graphene devices at which the Fermi level (E_F) of either the graphene or the graphite probe is aligned.^{9,19,20,22} Unlike conventional tunneling experiments with metal samples, however, E_F of graphene is also modulated while sweeping V_b and monitoring the tunneling signals, similar to the charge-density modulation of graphene with V_g through bottom *h*-BN and SiO₂ (either 290 or 90 nm in thickness) insulators. Thus, we can readily deduce the electronic structures of *h*-BN-graphene tunneling devices by controlling the Fermi-level positions of graphene and graphite probe and monitoring the tunneling signals as functions of V_g and V_b .

Figure 1a,b shows representative $G = dI/dV_b$ spectra from the single-layer and bilayer tunneling devices, respectively, at gate voltages of $V_g = -50$ to -40 V with a step of $\Delta V_g = 2$ V and $T = 5.0$ K. The differential conductance is found either by applying small AC-excitation voltage ($V_{rms} = 1$ mV) to DC sample bias or numerically obtained from the I - V_b curve. The most noticeable feature in dI/dV_b for the single-layer device

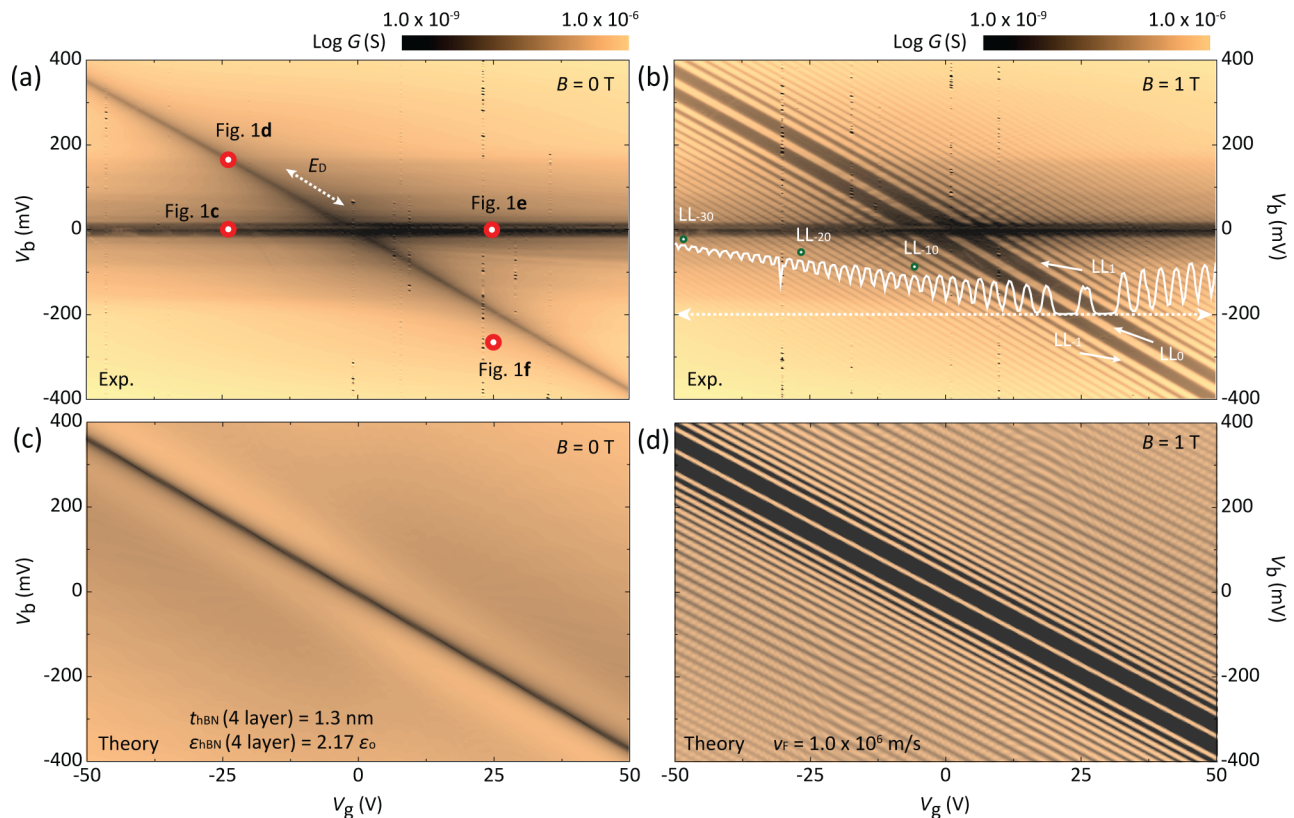


Figure 2. (a,b) High-resolution dI/dV_b gate mappings for the single-layer graphene device at $T = 5.0$ K, varying V_g from $V_g = -50$ to 50 V with a step of $\Delta V_g = 0.4$ V at (a) $B = 0$ T and (b) $B = 1$ T. The white overlaid plot in (b) is from the line cut at $V_b = -200$ mV, displaying over 30 well-separated LLs. (c,d) Simulated dI/dV_b gate mappings at (c) $B = 0$ T and (d) $B = 1$ T with the same geometric parameters as those in experiments. The relative permittivity of four-layer h -BN, the single variable for the gate-mapping simulation in (c), is found to be $\epsilon = 2.17 \epsilon_0$. The Fermi velocity of graphene (v_F), obtained from the LL spectra in the quantum Hall regime ((b) and (d)), is $v_F = 1.0 \times 10^6$ m/s.

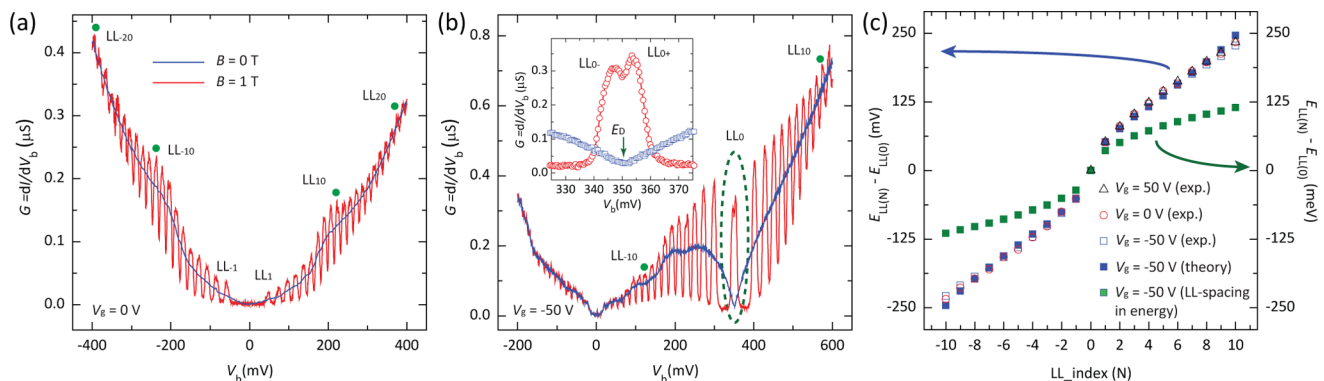


Figure 3. (a,b) High-resolution individual dI/dV_b spectra measured at (a) the charge neutral ($V_g = 0$ V) and (b) hole-doped ($V_g = -50$ V) regions. The well-separated conductance oscillations, each representing an individual LL, demonstrate the signal-to-noise ratio improvement in the h -BN-tunneling devices. The inset in (b) shows the LL_0 , developed at E_D is split into LL_{0-} and LL_{0+} peaks at $B = 1$ T. (c) LL-peak spacing with respect to LL_0 at different doping levels in V_b . Open symbols are from experimental data and closed blue squares from theoretical calculations with $v_F = 1.0 \times 10^6$ m/s. Closed green squares are the converted LL-peak spacing in energy at $V_g = -50$ V. Uncertainties for each data point are smaller than symbol sizes.

(Figure 1a) is the sharp dip around $V_b = 350$ mV, where E_F of the single layer graphene is aligned at E_D (Figure 1d). Contrasted to bilayer graphene (Figure 1b), the spectra gap is formed at E_D with a width of ≈ 45 mV at $V_g = -50$ V. We relate this spectra gap to the electric field-induced energy gap of bilayer graphene.²³

Much detailed information on the electronic structures of graphene can be found in a series of tunneling measurements while varying the charge density with V_g .^{9,19,20} As shown in

Figure 1a,b, we can separate dI/dV_b spectra into two types of tunneling features: one displaying charge density dependence and the other not. We have previously shown that the tunneling signals that do not display charge-density dependence can be related to inelastic electron tunneling events assisted by the phonon scatterings of graphene, h -BN, and graphite.¹⁵ However, the spectra displaying charge-density dependence are associated with the electronic structures of graphene. The discussions on these tunneling features such as E_D for single-

layer and E_g for bilayer graphene and the LLs formed in the quantum Hall regime are the main focus of this report.

Figure 2a,b shows the dI/dV_b gate mappings at $B = 0$ T and $B = 1$ T, respectively, which consist of 251 independent dI/dV_b spectra measured from $V_g = -50$ to 50 V with a spacing of $\Delta V_g = 0.4$ V for the single-layer device. At zero magnetic field, the positions of E_D can be easily identified as the dark line running diagonally across the map along with the conductance-suppressed region at E_F ($V_b = 0$ mV). This zero-bias anomaly at E_F is known as a characteristic feature of electron tunneling into graphene and other low-dimensional materials.^{24–26} Upon applying a perpendicular magnetic field, the electronic states in graphene collapse to quantized energy levels, referred to as LLs, and previous STS studies on those LLs demonstrate the versatility of tunneling experiments in the quantum Hall regime.^{9,19–21} Quite surprisingly, we can identify more than 40 LLs up to $LL_{\pm 30}$ in both electron- and hole-doped regions along with the $N = 0$ LL developed at the same location as E_D . The linear evolutions of higher index LLs with little variation in the tunneling-spectra spacing in V_b (Figure 2b) suggest that the electronic structures of h -BN-graphene tunneling devices remain unchanged over the measurement ranges of V_g and V_b .

Our measurements prove that the signal-to-noise ratio of the tunneling spectra can be significantly improved by employing the chemically and mechanically stable h -BN-tunnel junction, as demonstrated in the high-resolution dI/dV_b spectra in Figure 3a,b. The blue and red solid lines represent the differential conductance measured at $B = 0$ T and $B = 1$ T, respectively, for charge-neutral ($V_g = 0$ V, Figure 3a) and hole-doped ($V_g = -50$ V, Figure 3b) regions. Regarding the series of conductance-peak oscillations, each peak corresponds to an individual LL, clearly seen with the highest LL_0 dI/dV_b peak at E_D . We are able to observe LL formation as early as $B = 0.2$ T (Figure S1a) and a signature of symmetry breaking of LL_0 even at $B = 1$ T, as evidenced by the split conductance peaks displayed in the inset of Figure 3b. Here, note that LL spacing (Figures 2b and 3) converges to a constant value, especially at higher LL indices, as opposed to the theoretical expectation for single-layer graphene.²⁷ Because our tunneling spectra are displayed as a function of V_b , the intervals between adjacent LL peak positions in V_b exhibit distinct behavior from the LL spacing in energy. Consequently, careful analysis is necessary to account for the tunneling spectra in V_b for the electronic structures of graphene, as discussed in depth in later sections.

On account of the semimetallic nature of graphene, the positions of E_D (Figure 2a) and LLs (Figure 2b) in the $V_g - V_b$ 2D gate mapping are determined by not only the electronic structures of graphene but also the electrostatic interactions of the h -BN-graphene tunnel junction. The electrostatic interactions around the h -BN-graphene tunneling devices can be parametrized with the capacitance at the junction. The total capacitance $C_{\text{tot}} = (1/C_{\text{geo}} + 1/C_Q)^{-1}$ is determined by the geometrical capacitance (C_{geo}) of the junction and the quantum capacitance (C_Q) of the graphene layer.²⁸ The quantum capacitance $C_Q = q^2 ((dn)/(dE_F))$ reflects the density of states of graphene at E_F , which can be readily tuned by any external electric field.^{29,30} Here, n is the carrier density per unit area and q is electron charge. It has been demonstrated that, for example, the presence of the metallic STM tip can alter the local electronic structure of graphene by introducing additional charged carriers, accordingly shifting E_F .^{20,22}

In the planar tunneling junction, moreover, the geometric capacitance of the junction is much larger; consequently, its

contribution to the total capacitance becomes smaller than that of an atomic junction of STM because the area of the graphite- h -BN-graphene tunneling junction is several microns (Figure 1a inset). Thus, the quantum capacitance of graphene and the varying position of graphene E_F in response to external electric fields play a major role in deciding the tunneling spectra in h -BN-graphene tunneling devices. For example, when negative V_g is applied to the back-gate electrode, e.g., $V_g = -25$ V and $V_b = 0$ mV (bottom-left red dot in Figure 2a), the Fermi levels of graphene and probe are aligned lower than E_D (Figure 1c). Next, positive V_b on the graphite probe induces additional negative charges on the graphene through capacitive coupling, raising graphene E_F toward E_D . Once E_F of graphene is aligned at E_D (Figure 1d), differential conductance drops sharply in value. Similarly, negative V_b is required to align graphene E_F to E_D at positive V_g (Figure 1e,f).

The linear evolutions of E_D (Figure 2a) and LLs (Figure 2b) in the dI/dV_b gate mappings prove that the aforementioned planar capacitive model is sufficient to explain the spectrum features in our data. First, we find the locations of E_D (Figure 2a) in the $V_g - V_b$ gate mappings; E_D exists where the total induced charges $n_{\text{tot}} = C_g V_g + C_t V_b$ are equal to zero. Here

$C_g = \frac{\epsilon_{h\text{-BN}} \epsilon_{\text{SiO}_2}}{q(t_{h\text{-BN}} \epsilon_{\text{SiO}_2} + t_{\text{SiO}_2} \epsilon_{h\text{-BN}})}$ and $C_t = \frac{\epsilon_{h\text{-BN}}^T}{q t_{h\text{-BN}}^T}$ are geometric capacitances of the bottom SiO_2 - h -BN insulators and h -BN tunneling insulator, respectively. The capacitance of the back-gate C_g is predetermined by geometrical factors: thickness and relative permittivity of the bottom insulators of SiO_2 ($t_{\text{SiO}_2} = 290$ nm, $\epsilon_{\text{SiO}_2} = 3.9 \epsilon_0$) and h -BN ($t_{h\text{-BN}}^B = 30$ nm, $\epsilon_{h\text{-BN}}^{B,\text{bulk}} = 4.0 \epsilon_0$), where ϵ_0 is the vacuum permittivity. With tunneling insulator thickness $t_{h\text{-BN}}^T = 1.3$ nm–1.4 nm for four-layer h -BN,^{13,31} the only fitting parameter is the relative permittivity of the four-layer h -BN, found to be 54% ($\epsilon_{h\text{-BN}}^{T,4L} = 2.17 \epsilon_0$ for $t_{h\text{-BN}}^T = 1.3$ nm) of the value in bulk h -BN ($\epsilon_{h\text{-BN}}^{B,\text{bulk}} = 4.0 \epsilon_0$) (see the Supporting Information for detailed analysis).

With the attained relative permittivity of the h -BN insulator ($\epsilon_{h\text{-BN}}^{T,4L}$), the information on the electronic structures of single layer graphene, such as the Fermi velocity of charged carriers, can be obtained from the analysis of LL peak spacing in V_b . Figure 3c shows the LL peak positions in V_b with respect to LL_0 as a function of LL index for different gate voltages: electron-doped ($V_g = 50$ V), neutral ($V_g = 0$ V), and hole-doped ($V_g = -50$ V) regions. No noticeable differences are seen in LL spacing at the varying doping levels. The filled blue squares in Figure 3c are from the model calculation and a perfect agreement with experimental data is attained with $v_F = 1.0 \times 10^6$ m/s as the Fermi velocity of single-layer graphene.^{9,25,32} Using the relation between V_b and energy $E = s \hbar v_F \sqrt{\pi |C_g V_g + C_t V_b|}$ with $s = \pm 1$ for electron and hole-doped states, we convert the LL peak positions in V_b to the energy difference from the LL_0 , $E_{LLN} - E_{LL0}$, and plot them as closed green squares in Figure 3c. Using electron-tunneling transmission probability based on the WKB approach (see the Supporting Information), we simulate the dI/dV_b gate mappings for the single-layer device at $B = 0$ T (Figure 2c) and $B = 1$ T (Figure 2d), with the simulated results exhibiting outstanding agreement with the experimental observations. We estimate that the LL broadening originated from sample inhomogeneity to be around 1.5 meV (see the Supporting Information), which is consistent with disorders probed by STM measurements.^{20,33}

Next, we turn our attention to the tunneling spectra from bilayer graphene. Figure 4a shows the dI/dV_b gate mapping composed of 301 independent plots from $V_g = -60$ to 60 V with spacing of $\Delta V_g = 0.4$ V at $T = 5$ K. As discussed with the

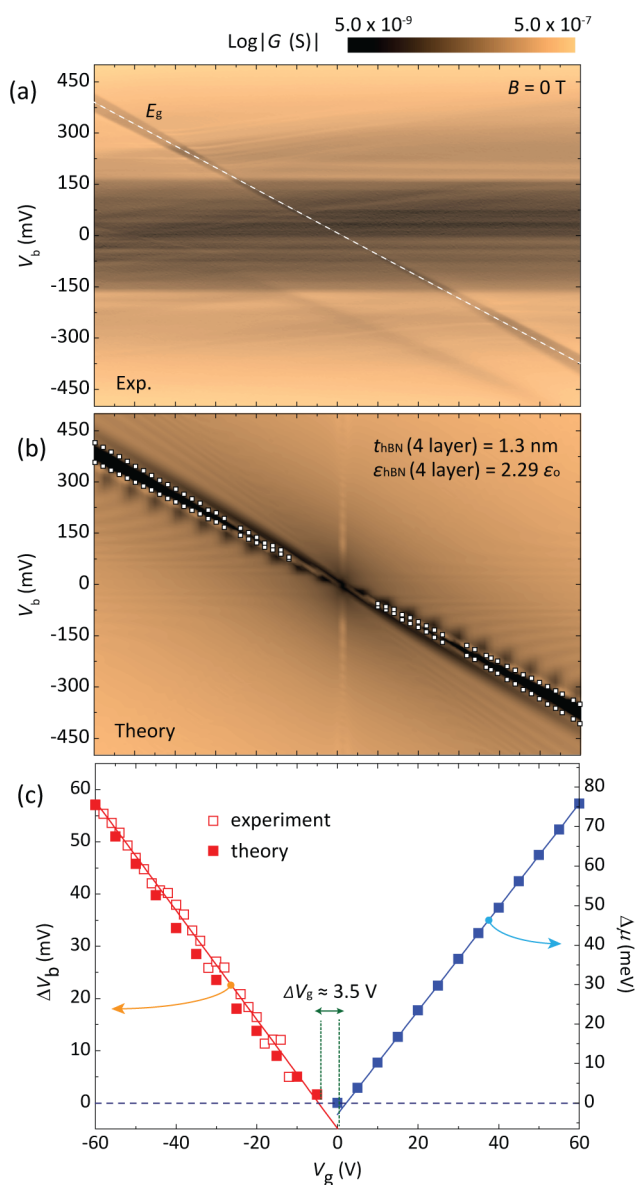


Figure 4. (a) High-resolution dI/dV_b gate mapping for the bilayer graphene device at $T = 5.0$ K, varying V_g from $V_g = -60$ to 60 V with a step of $\Delta V_g = 0.4$ V at $B = 0$ T. The spectra gap, directly linked to the electric field-induced bilayer energy gap, is identified as the diagonal shaded band where width and position change as functions of V_g and V_b . The white dashed line is from the device simulation locating the middle of the energy gap. (b) Simulated dI/dV_b gate mapping at $B = 0$ T. Overlaid white squares indicate spectra-gap boundaries extracted from experimental data in (a). The single variable for this gate-mapping simulation is the relative permittivity of four-layer h -BN, $\epsilon = 2.29 \epsilon_0$, based on the same geometric parameters as those in the corresponding experiment. (c) Open and closed red squares represent the variation of spectra-gap spacing in V_b as a function of V_g , extracted from experiment data (a) and theoretical calculation (b), respectively. Closed blue squares indicate the chemical potential difference ($\Delta\mu$) of the top and bottom graphene layers, which is the actual electric field-induced energy gap of bilayer graphene. Uncertainties for each data point are smaller than symbol sizes.

single-layer device, tunneling signals reflect not only the electronic structures of bilayer graphene but also the electrostatic interactions through the h -BN tunnel junction, as seen here in the electric field-induced energy gap, and the relative permittivity of a thin h -BN insulator. For example, the positions of E_D in the $V_g - V_b$ gate mappings are determined by device geometries, such as an h -BN tunneling insulator thickness, while being little-affected by the electronic structures of the bilayer graphene. Note that the transition of E_D (middle of the spectra gap) across the dI/dV_b gate mapping (Figure 4a) is similar to the location of E_D from the single-layer device (Figure 2a) because both devices have four-layer h -BN as a tunneling insulator. The dashed white line in Figure 4a locates the E_D obtained from model calculations with $\epsilon_{hBN}^{TAL} = 2.29 \epsilon_0$ as the relative permittivity of four-layer h -BN in the bilayer device.

As shown in Figure 4a, the spectra gap, originating from the electric field-induced energy gap of bilayer graphene,²³ opens where E_D is located and widens up to ≈ 60 mV at $V_g = \pm 60$ V and $V_b = \pm 350$ mV. The spectra gap size is obtained by locating the gap boundaries from the numerical fittings of the peak and dip positions in dG/dV_b (Figure 1c inset). To quantitatively compare the observed spectra gaps with the bilayer graphene energy gap, we calculate the accumulated charges on the top and bottom graphene layers and the electric field between them using the aforementioned electrostatic model. Because the energy band of bilayer graphene remains as a parabolic dispersion at low doping levels, the chemical potential difference ($\Delta\mu$) directly linked to the bilayer energy gap is obtained with $d = 0.335$ nm as the distance between graphene layers. The closed blue squares in Figure 4c represent $\Delta\mu$ from the model simulation (see the Supporting Information). Following the same WKB-based tunneling transmission formula, we simulated dI/dV_b gate mapping for the bilayer device (Figure 4b), which successfully reproduce the electric field-tunable energy gap of bilayer graphene. The open and closed red squares in Figure 4c are the spectra gaps from experiments and model calculations in V_b , respectively, which are consistently smaller than the actual energy gaps of bilayer graphene by as much as 30% (see the Supporting Information). In addition, we notice that the opening of the bilayer energy gaps requires additional charges from $\Delta V_g \approx 3.5$ V ($\Delta n \approx 2.6 \times 10^{11} \text{ cm}^{-2}$), which need to compensate for the opposite polarization of the bilayer energy-gap openings in the presence of electron–hole puddles.¹⁹

We move on to the discussion of the relative permittivity of thin h -BN film. To investigate the relation between the thickness and relative permittivity of h -BN film in detail, we have prepared several h -BN-graphene tunneling devices with varying h -BN thickness (see additional gate mappings in the Supporting Information). We limit our discussion to the devices with three to five h -BN layers^{13,31} for the following reasons. For samples with less than three h -BN layers, the tunneling resistance becomes smaller than the sheet resistance of graphene and graphite probe,^{34,35} which eventually determine the overall transport properties of the devices. When the h -BN insulator is thicker than five layers, the tunneling current becomes too small ($< 10^{-13}$ A/ μm^2) and is severely afflicted by measurement noise. Figure 5a summarizes how sensitive tunneling current is to the number of h -BN insulating layers. We normalize the tunneling current with the area of the tunneling junction, defined by the widths of graphene and graphite probe.

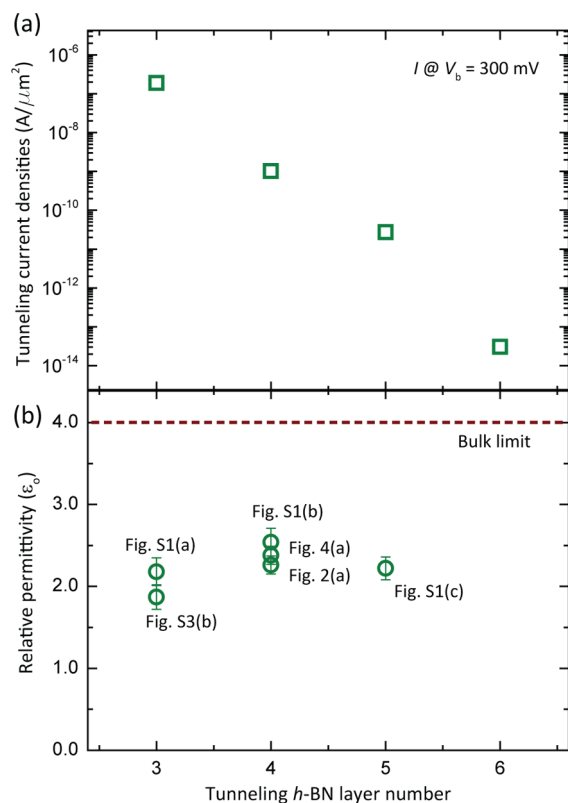


Figure 5. (a) Tunneling current densities normalized with the area of tunnel junctions at $V_b = 300$ mV and $T = 5.0$ K for varying thickness of h -BN tunneling insulator from three to six atomic layers. (b) Relative permittivities extracted from the model calculations in locating the charge neutrality point E_D in $V_g - V_b$ mappings for one bilayer and five single-layer graphene devices. The marked uncertainties are from thickness variations in both top and bottom h -BN insulators.

The relative permittivities for different h -BN insulator thicknesses are obtained from the model calculations in locating E_D in the $V_g - V_b$ gate mappings. As shown in Figure S5b, the relative permittivities of three-to-five layer h -BN films are consistently smaller than the value of bulk film: $\epsilon_{h\text{-BN}}^{3L} = (2.18 \pm 0.17) \epsilon_0$, $\epsilon_{h\text{-BN}}^{4L} = (2.54 \pm 0.17) \epsilon_0$, and $\epsilon_{h\text{-BN}}^{5L} = (2.22 \pm 0.14) \epsilon_0$ for three- (Figure S2b), four- (Figure S2c), and five-layer (Figure S 2d) h -BN, respectively. The marked uncertainties are linked to reported thickness variations of h -BN tunneling insulators: $t_{h\text{-BN}}^{3L} = 0.9$ to 1.0 nm, $t_{h\text{-BN}}^{4L} = 1.3$ to 1.4 nm, and $t_{h\text{-BN}}^{5L} = 1.8$ to 1.9 nm.^{13,31} Moreover, we take into account the thickness variation of the bottom h -BN insulator ($\Delta t_{h\text{-BN}}^{\text{bulk}} = \pm 10$ nm) as well to relieve other uncertainties that could be inflicted during the device fabrication process, such as air gaps formed at 2D-heterostructure interfaces. For a certain sample, we independently measure the back-gate C_g by the periodicity of the magnetoresistance oscillations from a conventional quantum Hall device, fabricated on the same h -BN and SiO_2 back-gate insulators as the h -BN-graphene tunneling device (Figure S3).

Even though the reduced relative permittivity, associated with a weakened screening capability of a thin h -BN insulating layer, is directly inferred from the quantitative analysis with experimental data and previous reports on other 2D materials such as graphene and MoS_2 thin films,^{36–38} direct accountabilities on the relative permittivity of atomically thin insulating film still remain unclear. For example, Gang et al. reported that the relative permittivity of CVD-grown h -BN films increased

upon decreasing film thickness ($\epsilon_{h\text{-BN}} = (6.8 \pm 0.9) \epsilon_0$ for four-layer h -BN).³⁹ We cautiously claim that the opposite results in the present work could be due to the dissemblance of our atomically clean graphene- h -BN tunnel junctions with their CVD-grown h -BN-Au junctions, not to mention the quality difference of h -BN films: single-crystalline h -BN versus CVD-grown h -BN. Supporting our claims, Li et al. studied the dielectric screening of high-quality h -BN films using electric force microscopy and density functional theory and concluded that the relative permittivity of thin h -BN films indeed decreased with a weak dependence on layer thickness,⁴⁰ as consistent with our observations (Figure S5b).

In summary, the electronic structures of single and bilayer graphene were probed by electron tunneling spectroscopy measurements with and without external magnetic fields, exploiting chemically and mechanically stable h -BN-2D tunnel junctions with exceptionally high signal-to-noise ratio. The tunneling spectra related to the E_D and the opening of electric field-induced bilayer energy gap were directly measured. In the quantum Hall regime, the development of LLs was seen as early as 0.2 T, with as many as $\text{LL}_N = \pm 30$ observed for both electron- and hole-doped regions. The electrostatic interactions through the h -BN tunneling insulator are sufficient to explain the experimental observations from single and bilayer tunneling devices. Additionally, we extracted the relative permittivity of three-to-five layer h -BN films and found that the screening capability of thin h -BN films was weakened significantly. We claim that our measurement is the most-accurate assessment to date for the relative permittivity of thin insulating layers, free of any structural defects or chemical disorder influence. Our experiments demonstrated that electron-tunneling spectroscopy measurements with h -BN tunneling devices can be an outstanding experimental platform for investigating various physical properties of nanoscale systems, not only for graphene but also for other low-dimensional materials.

Methods. h -BN-graphene tunneling devices are fabricated with multiple steps of the dry-transfer method.¹⁰ First, bottom thick h -BN (>20 nm) is mechanically exfoliated from high-quality single crystals and transferred onto thermally grown 290 or 90 nm thick SiO_2 on Si. We carefully examine surface cleanliness with a dark-filtered optical microscope and an atomic force microscope to select defect-free substrates. Before exfoliation of the h -BN flakes, SiO_2 -Si substrates are thoroughly cleaned with solvents in an ultrasonication bath and dipped in piranha solution. Second, either single-layer or bilayer graphene is transferred on top of the bottom h -BN flakes. To do this, we prepare the Si substrates, spin-coated with water-soluble poly-styrene sulfonic (PSS) acid and poly(methyl methacrylate) (PMMA). The thicknesses of PSS and PMMA films are carefully adjusted for better optical contrast to identify the number of graphene layers.^{41,42} Desirable flakes mechanically exfoliated from either natural graphite or HOPG on the polymer-stacked Si substrates are examined under an optical microscope and later transferred to predefined locations in the micromanipulating transfer stage. For some devices, we patterned graphene films into graphene ribbons with widths of a few microns, utilizing electron-beam lithography and dry-etching procedures. After dissolving PMMA in warm acetone (60°C), we anneal the samples in a mixture of Ar and H_2 (9:1 ratio by flow rate) at an elevated temperature (350°C) for more than 4 h to further remove any polymer residues and reduce the number of bubbles formed in the 2D heterostructures. Next, thin h -BN (three to five layers) and graphite

flakes are sequentially transferred on top of the graphene-bottom *h*-BN surfaces with the aforementioned dry-transfer methods using PSS-PMMA polymer stacks. Before the transfer of the graphite flakes, the samples are annealed again to ensure a disorder-free graphite-*h*-BN interface. Finally, conventional electron-beam lithography and the metal lift-off process are used to fabricate the Ti-Au (5 nm/55 nm) electrodes.

■ ASSOCIATED CONTENT

Supporting Information

The Supporting Information is available free of charge on the ACS Publications website at DOI: 10.1021/acs.nanolett.6b03821.

Additional gate mappings from the single-layer graphene device in the quantum Hall regime and data from other single-layer tunneling devices with varying *h*-BN thickness. Models and formalisms of the theoretical calculations supporting the analysis of the experimental results, e.g., the tunneling mechanisms, the opening a gap of bilayer graphene, and Landau level formations. (PDF)

■ AUTHOR INFORMATION

Corresponding Authors

*E-mail: syjung@kriss.re.kr.

*E-mail: hcpark@ibs.re.kr.

ORCID

Suyong Jung: 0000-0003-3885-9999

Author Contributions

S. J. and N. M. contributed to this work equally.

Notes

The authors declare no competing financial interest.

■ ACKNOWLEDGMENTS

We acknowledge P. Moon, Y.-W. Son, J. Jung, J. Suh, I. H. Lee, N. Zhitenev, and J. A. Stroscio for fruitful discussions and comments on the manuscript. This work has been supported by Nano-Material Technology Development Program through the National Research Foundation of Korea (NRF) funded by the Ministry of Science, ICT, and Future Planning (2012M3A7B4049888). Support also came from project code IBS-R024-D1 as well as by the Korea-Hungary joint laboratory program for Nanosciences through the National Research Council of Science and Technology.

■ REFERENCES

- (1) Wolf, E. L. *Principles of Electron Tunneling Spectroscopy*; Oxford University Press: New York, 1989.
- (2) Giaever, I. Energy Gap in Superconductors Measured by Electron Tunneling. *Phys. Rev. Lett.* **1960**, *5*, 147–148.
- (3) Giaever, I. Electron Tunneling between Two Superconductors. *Phys. Rev. Lett.* **1960**, *5*, 464–466.
- (4) Hashimoto, K.; Sohrmann, C.; Wiebe, J.; Inaoka, T.; Meier, F.; Hirayama, Y.; Römer, R. A.; Wiesendanger, R.; Morgenstern, M. Quantum Hall Transition in Real Space: From Localized to Extended States. *Phys. Rev. Lett.* **2008**, *101*, 256802.
- (5) Li, G.; Andrei, E. Y. Observation of Landau Levels of Dirac Fermions in Graphite. *Nat. Phys.* **2007**, *3*, 623–627.
- (6) Li, G.; Luican, A.; Andrei, E. Y. Scanning Tunneling Spectroscopy of Graphene on Graphite. *Phys. Rev. Lett.* **2009**, *102*, 176804.
- (7) Song, Y. J.; Otte, A. F.; Kuk, Y.; Hu, Y.; Torrance, D. B.; First, P. N.; de Heer, W. A.; Min, H.; Adam, S.; Stiles, M. D.; MacDonald, A. H.; Stroscio, J. A. High-Resolution Tunneling Spectroscopy of a Graphene Quartet. *Nature* **2010**, *467*, 185–189.
- (8) Binnig, G.; Rohrer, H. Scanning Tunneling Microscopy—from Birth to Adolescence. *Rev. Mod. Phys.* **1987**, *59*, 615.
- (9) Jung, S.; Rutter, G. M.; Klimov, N. N.; Newell, D. B.; Calizo, I.; Hight-Walker, A. R.; Zhitenev, N. B.; Stroscio, J. A. Evolution of Microscopic Localization in Graphene in a Magnetic Field from Scattering Resonances to Quantum Dots. *Nat. Phys.* **2011**, *7*, 245–251.
- (10) Dean, C. R.; Young, A. F.; Meric, I.; Lee, C.; Wang, L.; Sorgenfrei, S.; Watanabe, K.; Taniguchi, T.; Kim, P.; Shepard, K. L.; Hone, J. Boron Nitride Substrates for High-Quality Graphene Electronics. *Nat. Nanotechnol.* **2010**, *5*, 722–726.
- (11) Geim, A. K.; Grigorieva, I. V. Van der Waals Heterostructures. *Nature* **2013**, *499*, 419–425.
- (12) Britnell, L.; Gorbachev, R. V.; Geim, A. K.; Ponomarenko, L. A.; Mishchenko, A.; Greenaway, M. T.; Fromhold, T. M.; Novoselov, K. S.; Eaves, L. Resonant Tunneling and Negative Differential Conductance in Graphene Transistors. *Nat. Commun.* **2013**, *4*, 1794.
- (13) Britnell, L.; Gorbachev, R. V.; Jalil, R.; Belle, B. D.; Schedin, F.; Katsnelson, M. I.; Eaves, L.; Morozov, S. V.; Mayorov, A. S.; Peres, N. M. R.; Castro Neto, A. H.; Leist, J.; Geim, A. K.; Ponomarenko, L. A.; Novoselov, K. S. Electron Tunneling through Ultrathin Boron Nitride Crystalline Barriers. *Nano Lett.* **2012**, *12*, 1707–1710.
- (14) Britnell, L.; Gorbachev, R. V.; Jalil, R.; Belle, B. D.; Schedin, F.; Mishchenko, A.; Georgiou, T.; Katsnelson, M. I.; Eaves, L.; Morozov, S. V.; Peres, N. M. R.; Leist, J.; Geim, A. K.; Novoselov, K. S.; Ponomarenko, L. A. Field-Effect Tunneling Transistor Based on Vertical Graphene Heterostructures. *Science* **2012**, *335*, 947–950.
- (15) Jung, S.; Park, M.; Park, J.; Jeong, T.-Y.; Kim, H.-J.; Watanabe, K.; Taniguchi, T.; Ha, D. H.; Hwang, C.; Kim, Y.-S. Vibrational Properties of *h*-BN and *h*-BN-Graphene Heterostructures Probed by Inelastic Electron Tunneling Spectroscopy. *Sci. Rep.* **2015**, *5*, 16642.
- (16) Mishchenko, A.; Tu, J. S.; Cao, Y.; Gorbachev, R. V.; Wallbank, J. R.; Greenaway, M. T.; Morozov, V. E.; Morozov, S. V.; Zhu, M. J.; Wong, S. L.; Withers, F.; Woods, C. R.; Kim, Y.-J.; Watanabe, K.; Taniguchi, T.; Vdovin, E. E.; Makarovskiy, O.; Fromhold, T. M.; Fal'ko, V. I.; Geim, A. K.; Novoselov, K. S.; Eaves, L. Twist-Controlled Resonant Tunneling in Graphene/Boron Nitride/Graphene Heterostructures. *Nat. Nanotechnol.* **2014**, *9*, 808–813.
- (17) Withers, F.; Del Pozo-Zamudio, O.; Mishchenko, A.; Rooney, A. P.; Gholinia, A.; Watanabe, K.; Taniguchi, T.; Haigh, S. J.; Geim, A. K.; Tartakovskii, A. I.; Novoselov, K. S. Light-Emitting Diodes by Band-Structure Engineering in van der Waals Heterostructures. *Nat. Mater.* **2015**, *14*, 301–306.
- (18) Vdovin, E. E.; Mishchenko, A.; Greenaway, M. T.; Zhu, M. J.; Ghazaryan, D.; Misra, A.; Cao, Y.; Morozov, S. V.; Makarovskiy, O.; Fromhold, T. M.; Patanè, A.; Slotman, G. J.; Katsnelson, M. I.; Geim, A. K.; Novoselov, K. S.; Eaves, L. Phonon-Assisted Resonant Tunneling of Electrons in Graphene-Boron Nitride Transistors. *Phys. Rev. Lett.* **2016**, *116*, 186603.
- (19) Rutter, G. M.; Jung, S.; Klimov, N. N.; Newell, D. B.; Zhitenev, N. B.; Stroscio, J. A. Microscopic Polarization in Bilayer Graphene. *Nat. Phys.* **2011**, *7*, 649–655.
- (20) Chae, J.; Jung, S.; Young, A. F.; Dean, C. R.; Wang, L.; Gao, Y.; Watanabe, K.; Taniguchi, T.; Hone, J.; Shepard, K. L.; Kim, P.; Zhitenev, N. B.; Stroscio, J. A. Renormalization of the Graphene Dispersion Velocity Determined from Scanning Tunneling Spectroscopy. *Phys. Rev. Lett.* **2012**, *109*, 116802.
- (21) Luican-Mayer, A.; Kharitonov, M.; Li, G.; Lu, C.; Skachko, I.; Gonçalves, A. B.; Watanabe, K.; Taniguchi, T.; Andrei, E. Y. Screening Charged Impurities and Lifting the Orbital Degeneracy in Graphene by Populating Landau Levels. *Phys. Rev. Lett.* **2014**, *112*, 36804.
- (22) Zhao, Y.; Wyrick, J.; Natterer, F. D.; Rodriguez-Nieva, J. F.; Lewandowski, C.; Watanabe, K.; Taniguchi, T.; Levitov, L. S.; Zhitenev, N. B.; Stroscio, J. A. Creating and Probing Electron Whispering-Gallery Modes in Graphene. *Science* **2015**, *348*, 672–675.
- (23) Castro, E. V.; Novoselov, K. S.; Morozov, S. V.; Peres, N. M. R.; dos Santos, J. M. B. L.; Nilsson, J.; Guinea, F.; Geim, A. K.; Castro Neto, A. H. Biased Bilayer Graphene: Semiconductor with a Gap Tunable by the Electric Field Effect. *Phys. Rev. Lett.* **2007**, *99*, 216802.

- (24) Rutter, G. M.; Crain, J. N.; Guisinger, N. P.; Li, T.; First, P. N.; Stroscio, J. A. Scattering and Interference in Epitaxial Graphene. *Science* **2007**, *317*, 219–222.
- (25) Zhang, Y.; Brar, V. W.; Wang, F.; Girit, C.; Yayon, Y.; Panlasigui, M.; Zettl, A.; Crommie, M. F. Giant Phonon-Induced Conductance in Scanning Tunneling Spectroscopy of Gate-Tunable Graphene. *Nat. Phys.* **2008**, *4*, 627–630.
- (26) Efros, A. L.; Shklovskii, B. I. Coulomb Gap and Low Temperature Conductivity of Disordered Systems. *J. Phys. C: Solid State Phys.* **1975**, *8*, L49–L51.
- (27) Das Sarma, S.; Adam, S.; Hwang, E. H.; Rossi, E. Electronic Transport in Two-Dimensional Graphene. *Rev. Mod. Phys.* **2011**, *83*, 407–470.
- (28) Yu, G. L.; Jalil, R.; Belle, B.; Mayorov, A. S.; Blake, P.; Schedin, F.; Morozov, S. V.; Ponomarenko, L. A.; Chiappini, F.; Wiedmann, S.; Zeitler, U.; Katsnelson, M. I.; Geim, A. K.; Novoselov, K. S.; Elias, D. C. Interaction Phenomena in Graphene Seen through Quantum Capacitance. *Proc. Natl. Acad. Sci. U. S. A.* **2013**, *110*, 3282–3286.
- (29) Luryi, S. Quantum Capacitance Devices. *Appl. Phys. Lett.* **1988**, *52*, 501.
- (30) Lu, C.-P.; Li, G.; Mao, J.; Wang, L.-M.; Andrei, E. Y. Bandgap, Mid-Gap States, and Gating Effects in MoS₂. *Nano Lett.* **2014**, *14*, 4628–4633.
- (31) Chandni, U.; Watanabe, K.; Taniguchi, T.; Eisenstein, J. P. Evidence for Defect-Mediated Tunneling in Hexagonal Boron Nitride-Based Junctions. *Nano Lett.* **2015**, *15*, 7329–7333.
- (32) Martin, J.; Akerman, N.; Ulbricht, G.; Lohmann, T.; Smet, J. H.; von Klitzing, K.; Yacoby, A. Observation of Electron-Hole Puddles in Graphene Using a Scanning Single-Electron Transistor. *Nat. Phys.* **2008**, *4*, 144–148.
- (33) Xue, J.; Sanchez-Yamagishi, J.; Bulmash, D.; Jacquod, P.; Deshpande, A.; Watanabe, K.; Taniguchi, T.; Jarillo-Herrero, P.; LeRoy, B. J. Scanning Tunneling Microscopy and Spectroscopy of Ultra-Flat Graphene on Hexagonal Boron Nitride. *Nat. Mater.* **2011**, *10*, 282–285.
- (34) Zhang, Y.; Small, J. P.; Amori, M. E. S.; Kim, P. Electric Field Modulation of Galvanomagnetic Properties of Mesoscopic Graphite. *Phys. Rev. Lett.* **2005**, *94*, 176803.
- (35) Kim, Y.; Yun, H.; Nam, S.-G.; Son, M.; Lee, D. S.; Kim, D. C.; Seo, S.; Choi, H. C.; Lee, H.-J.; Lee, S. W.; Kim, J. S. Breakdown of the Interlayer Coherence in Twisted Bilayer Graphene. *Phys. Rev. Lett.* **2013**, *110*, 96602.
- (36) Datta, S. S.; Strachan, D. R.; Mele, E. J.; Johnson, A. T. C. Surface Potentials and Layer Charge Distributions in Few-Layer Graphene Films. *Nano Lett.* **2009**, *9*, 7–11.
- (37) Castellanos-Gomez, A.; Cappelluti, E.; Roldán, R.; Agraït, N.; Guinea, F.; Rubio-Bollinger, G. Electric-Field Screening in Atomically Thin Layers of MoS₂: The Role of Interlayer Coupling. *Adv. Mater.* **2013**, *25*, 899–903.
- (38) Cheiwchanchamnangij, T.; Lambrecht, W. R. L. Quasiparticle Band Structure Calculation of Monolayer, Bilayer, and Bulk MoS₂. *Phys. Rev. B: Condens. Matter Mater. Phys.* **2012**, *85*, 205302.
- (39) Shi, G.; Hanlunyuang, Y.; Liu, Z.; Gong, Y.; Gao, W.; Li, B.; Kono, J.; Lou, J.; Vajtai, R.; Sharma, P.; Ajayan, P. M. Boron Nitride-Graphene Nanocapacitor and the Origins of Anomalous Size-Dependent Increase of Capacitance. *Nano Lett.* **2014**, *14*, 1739–1744.
- (40) Li, L. H.; Santos, E. J. G.; Xing, T.; Cappelluti, E.; Roldán, R.; Chen, Y.; Watanabe, K.; Taniguchi, T. Dielectric Screening in Atomically Thin Boron Nitride Nanosheets. *Nano Lett.* **2015**, *15*, 218–223.
- (41) Blake, P.; Hill, E. W.; Castro Neto, A. H.; Novoselov, K. S.; Jiang, D.; Yang, R.; Booth, T. J.; Geim, A. K. Making Graphene Visible. *Appl. Phys. Lett.* **2007**, *91*, 63124.
- (42) Gorbachev, R. V.; Riaz, I.; Nair, R. R.; Jalil, R.; Britnell, L.; Belle, B. D.; Hill, E. W.; Novoselov, K. S.; Watanabe, K.; Taniguchi, T.; Geim, A. K.; Blake, P. Hunting for Monolayer Boron Nitride: Optical and Raman Signatures. *Small* **2011**, *7*, 465–468.